Solidification crack propagation and morphology dependence on processing parameters in AA6061 from ultra-high-speed x-ray visualization

Nadia Kouraytem^a, Po-Ju Chiang^b, Runbo Jiang^b, Christopher Kantzos^b, Joseph Pauza^b, Ross Cunningham^b, Ziheng Wu^b, Guannan Tang^b, Niranjan Parab^c, Cang Zhao^c, Kamel Fezzaa^c, Tao Sun^{c1}, Anthony D. Rollett ^{b*}

Abstract:

Solidification or hot cracks are commonly observed defects in a number of metal alloys and may lead to deterioration of additively manufactured parts quality. In this study, ultra-high-speed x-ray radiography experiments enable the observation and characterization of bundles of hot-cracks that form in monobloc AA6061 substrate. The crack bundles are related to meltpool characteristics and pore formation. Crack propagation rate is also presented for the case of a crack that initiates from a pore. Two types of relevant pore formation are also described, namely keyhole porosity and crack-remelting porosity. The results of this study are expected to facilitate the validation of theoretical and numerical models of solidification cracking.

Keywords: Solidification Hot Cracking, Dynamic X-ray Radiography, Metal Additive Manufacturing, Heterogeneous Nucleation

1 Introduction

- 2 Solidification- or hot-cracking (also known as hot-tearing or fissuring) in metallic
- 3 parts is one of the major concerns in manufacturing especially in casting, welding,
- 4 and, more recently, additive manufacturing. Cracking may develop in some alloys due
- to the rapid solidification and is detrimental to part performance, especially for
- 6 structural components that are subjected to loading. Reworking the part with cracks
 - constitutes a waste of time and resources and vet is unlikely to achieve the desired
- 8 result. Therefore, crack mitigation driven by the understanding of crack formation
- 9 mechanisms is crucial for manufacturing crack-free metallic parts.
- In laser powder bed fusion (LPBF) additive manufacturing, a part is printed in a layer-by-layer fashion by scanning a laser that selectively melts each layer of

^a Department of Mechanical and Aerospace Engineering, Utah State University, Logan, UT, USA:

^b Department of Materials Science and Engineering, Carnegie Mellon University, Pittsburgh, PA, USA;

^cX-ray Science Division, Advanced Photon Source, Argonne National Laboratory, Lemont, IL, USA

^{*}Professor Anthony D. Rollett
Department of Materials Science and Engineering
Carnegie Mellon University, 5000 Forbes Avenue, Pittsburgh, PA 15213-3890
Email: rollett@andrew.cmu.edu

^{1&}lt;sup>1</sup> Current address: Department of Materials Science and Engineering, University of Virginia, Charlottesville, VA 22904

powders. Despite the tremendous potential, relatively few alloys can be reliably printed using LPBF. This is largely because of the inconsistency in LPBF machines and a lack of understanding of the LPBF process, which may result in defects in the printed parts, such as keyhole porosity [1–7], lack of fusion porosity [5,8–10], balling [11–14], or solidification hot cracking [15–25]. Hot-cracking defects are identified in a number of metallic systems such as aluminum and nickel-based alloys. The main cause of hot-cracking in these alloys is the existence of a large mushy zone, the size of which is related to the wide freezing range from liquidus and solidus. Relevant to solidification cracking is in particular the freezing range from coherency to rigidity temperatures [26]. The main cause of hot-cracking in these alloys is the existence of a large mushy zone. During solidification of the melt pool, microsegregation may occur following the centerline of the laser scan path and at the grain boundaries. and A solidification crack hence initiates above the solidus temperature and propagates in the interdendritic liquid film. A number of mechanisms and criteria have been proposed to explain the hot-cracking phenomenon. A number of articles in the literature have looked at the hot-cracking problem in Aluminum alloys [27,28]. The reviews by Katgerman and Eskin [26,29] are particularly pertinent.

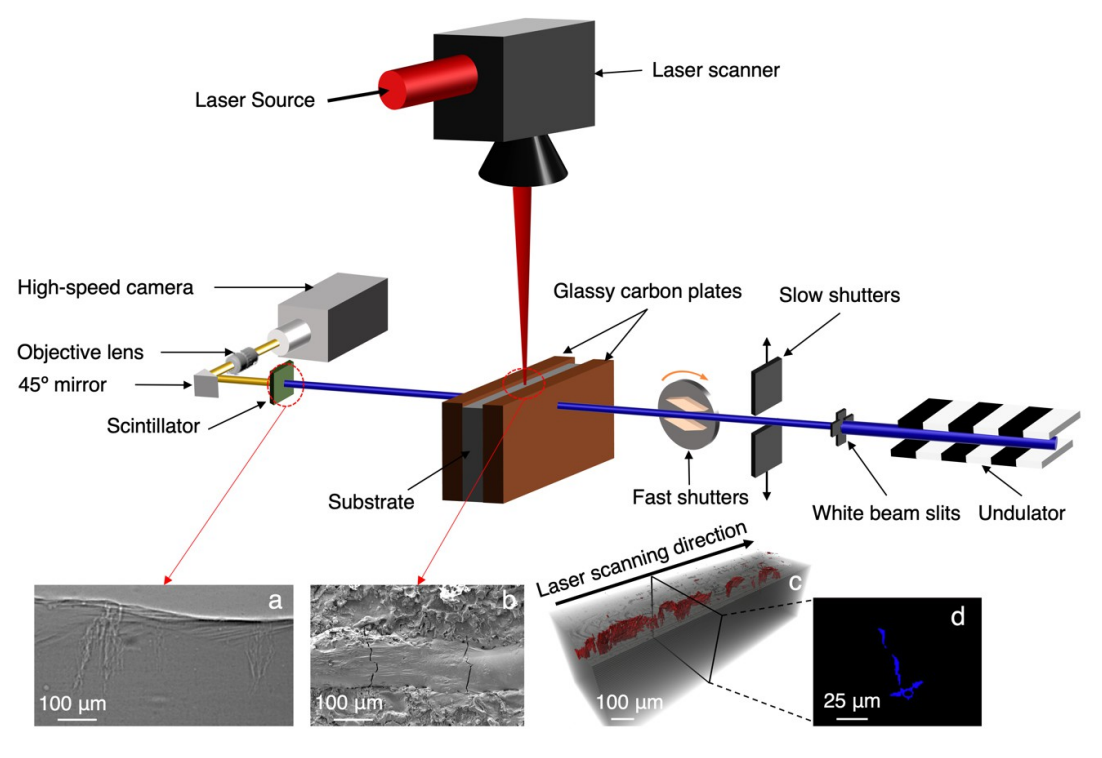
Both the material composition and processing parameters affect the formation and severity of hot cracking. The alloying elements influence the freezing range as well as the grain size and morphology, while the processing parameters determine the cooling rate and melt pool geometry. The strain rate that the material exhibits in the mushy zone is a commonly adopted criterion for predicting hot cracking [30,31], which has been combined with phase evolution during solidification in simulation efforts to characterize hot cracking under different processing parameters [32,33]. However, experimental observations are needed for supporting the theoretical models require and validating the predicted results. Owing to the opacity of metals, most experimental efforts have been limited to optical imaging of the surface of the melt pool and post-analysis of the sectioned samples (e.g., [32,34,35]).

In a highly dynamic solidification process such as that in LPBF, *in situ* experimental characterization of the melt pool geometry, bubble movement, and the initiation of cracking, which occur mostly beneath the surface [36], was not possible until the recent introduction of ultra-high speed visualization with synchrotron x-rays. Dynamic X-ray Radiography (DXR), a technique developed at the Advanced Photon Source at Argonne National Laboratory, has superior temporal and spatial resolutions up to 10 MHz and 1 µm, respectively [37]. These unique capabilities enabled the capturing of the highly dynamic melt pool motion, keyhole formation, particle spattering [7,38–40], pore generation [7], and solidification leading to hot-cracking [36].

By far, direct observations of the hot-cracking process via *in situ* experiments are still limited [24,25,41], mostly for aluminum alloy 6061 (AA6061). In this work, an *in situ* experimental investigation of hot cracking susceptibility in AA6061 using the DXR technique is presented. Laser melting in both spot weld and scanning modes under various processing parameters pertaining to metal additive manufacturing are discussed. Quantitative analysis of the crack bundles (length, width, and spacing between consecutive bundles) is performed and linked back to the melt pool depth, followed by the measurement of crack propagation. The formation of keyhole porosity, followed by hot-cracking, and porosity from a remelted crack will also be described.

61 Results and Discussion

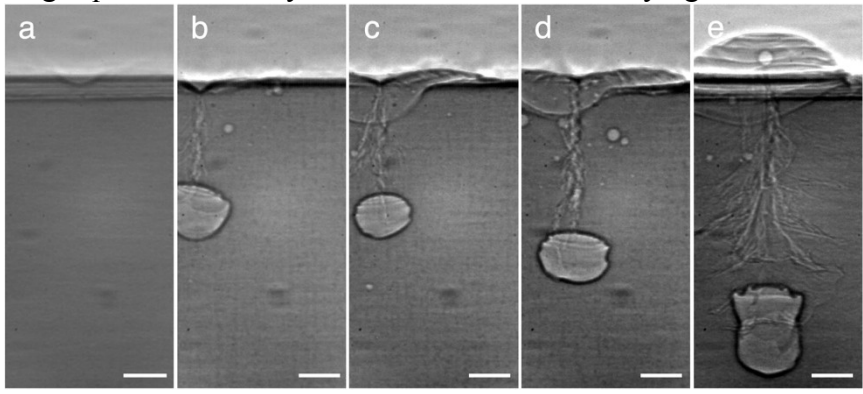
When examined from the sample surface using scanning electron microscopy (SEM), two representative cracks are apparent on the surface in the laser melted track, which is the wide horizontal feature with a relatively smooth surface, as seen in Error: Reference source not found (b). The cracks are continuous through the thickness of the sample and transverse, that is, perpendicular to the laser scanning direction, as determined from X-ray computed tomography in Error: Reference source not found (c). A number of cracks are observed within any given laser track, which allows distance to be measured between consecutive cracks. Even though the structure and morphology of the cracks appear simple in the top-view SEM image, DXR reveals that the crack morphology is much more complex beneath the surface Fig. 1 (a), which we now characterize under different processing parameters of spot welding and laser scanning.



Stationary laser

A series of spot weld experiments (i.e., stationary laser melting), wherein a selected power level of the laser was directed at the sample surface for a chosen dwell time, were conducted to investigate the influence of the thermal energy input on the hot cracking behavior. While in conduction mode (lower energy input), the vapor depression remained shallow and semicircular in shape without the formation of cracks, Error: Reference source not found (a). Operating in conduction mode is impractical in terms of printing efficiency and may lead to the formation of lack of fusion defects. However, a higher energy input induced the keyhole mode, and the vapor depression evolved to a deep, conical shape, leaving a pore behind after the laser was turned off, Error: Reference source not found (b-e). The morphology of the corresponding crack evolves from a bundle of vertical sub-cracks to an entangled and branched network as the laser power increases, consistent with the increased size

of the melt pool. Note the layered progression of the solidification of the substantial amount of liquid that is ejected from the keyhole, which is also evident at the top of the bubble surface. We speculate that the layering is caused by cycles of thermal shrinkage of the skin of solidifying metal around the circumference causing uplift of the remaining liquid followed by re-formation of the solidifying skin.



Scanning laser

89

90

91 92

93

94 95

96

97

98 99

100

101

102103

104

105106

107

108

109

110111

112

113

114115

116

117

118119

In the case of scanning laser melting, cracks also appear as bundles, and the crack length increases with the thermal energy input. The x-ray radiographs of the crack bundles under five different combinations of power and speed are shown in Fig. 3 (a-e). Clearly the hot cracking behavior is largely influenced by the processing parameters. Even though the crack bundles are three-dimensional in nature, as shown in Error: Reference source not found (d), it is important to be aware that DXR imaging only allows for resolving the two-dimensional projection as the absorption contrast is through the whole substrate thickness.

Three parameters are identified to describe crack bundles, namely the length and width of the crack bundles, along with the spacing between crack bundles that appear during a given laser scan, Fig. 3 (f-g). From analysis of the DXR images, the largest spans in each of the vertical and horizontal directions of each crack bundle are taken as the length and width, respectively. The spacing is defined here as the center-tocenter distance between a crack bundle to the adjacent one. Fig. 3 (f-g) presents the crack spacing (Fig. 3 (f)) and dimension (Fig. 3 (g)) of the bundle plotted against the linear energy density. Despite the large variation in crack spacing, Fig. 3 (f), the general trend is that crack bundles occur more frequently with increasing linear energy density. Figure 3 (g) shows that the length and width of the crack bundles both show an increasing trend with the linear energy density. Indeed, the depth of the melt pool, which is also plotted in Fig. 3 (g), demonstrates that no crack has extended beyond its corresponding melt pool depth along the vertical dimension. The average lengths of the crack bundles reach 65~79 % of their corresponding melt pool depth. Note that the large spread in values reflects the stochastic nature of the hot cracking process.

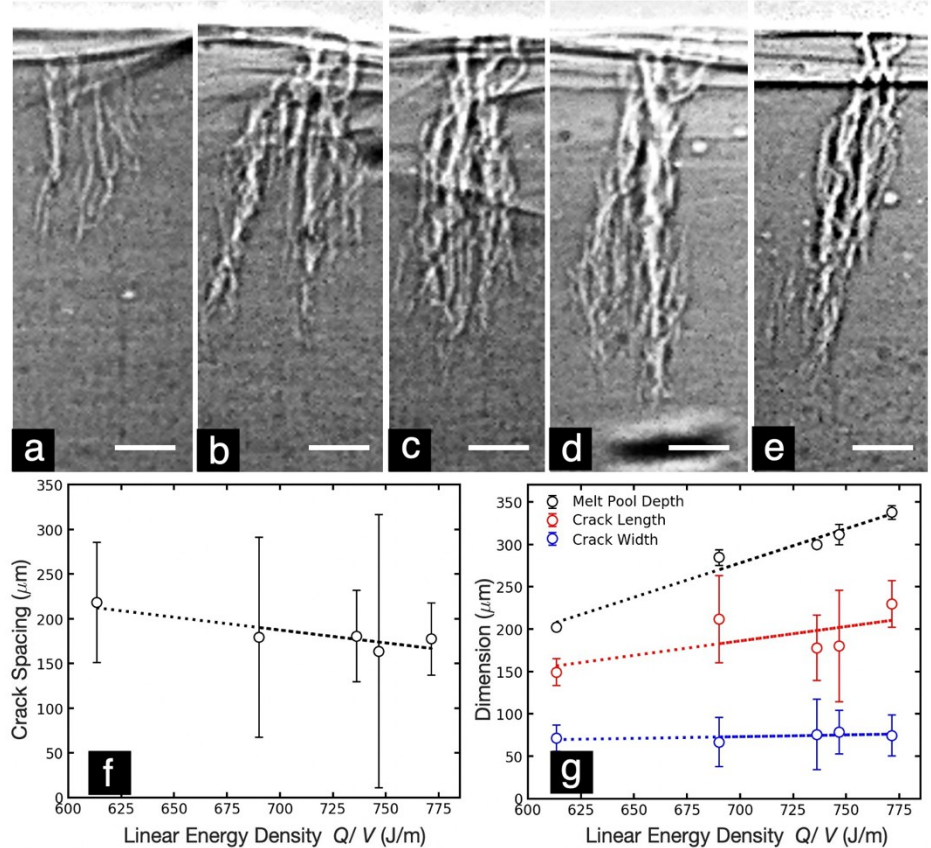


Figure 3. DXR images of the hot-crack bundles and measurements of hot-cracking parameters versus linear energy density: DXR images exhibiting the most significant crack bundles generated by a scanning laser with **a**) power 368 W, scan speed 0.6 m/s, energy density 613.3 J/m, **b**) power 368 W, scan speed 0.5 m/s, energy density 736 J/m, **c**) power 448 W, scan speed 0.6 m/s, energy density 746.7 J/m, **d**) power 540 W, scan speed 0.7 m/s, energy density 771.4 J/m. **e**) power 483 W, scan speed 0.7 m/s, energy density 690 J/m. The scale bar is 50 μm. Measurement of crack bundle spacing and dimension versus linear energy density. The error bar represents one standard deviation. **f**) Crack bundle spacing plotted versus linear energy density. The spacing is taken as the distance between the center of adjacent crack bundles. **g**) The crack bundle length and width plotted versus linear energy density, while the melt pool depth in each condition is also included. The dimension of each crack bundle is measured from the DXR images, and the largest span in vertical and horizontal direction of each bundle is regarded as the crack bundle length and width, respectively.

The crack propagation is observed to be intergranular in nature. One example of a cross-sectional view of the solidified meltpool (traced using a red dash-dotted line) containing a hot crack is show in Fig. 4 (a) and shown with higher resolution in Fig. 4(b), as seen under SEM. Inverse pole figure (IPF) maps of the high-resolution area of interest is shown in Fig. 4(c). Grain boundaries are drawn in black for misorientation angles of more than 6°. It is observed that the crack propagates in an intergranular fashion where the two branches of the crack are expected to be two different initiation points that converge to the same point at the upper portion of the substrate.

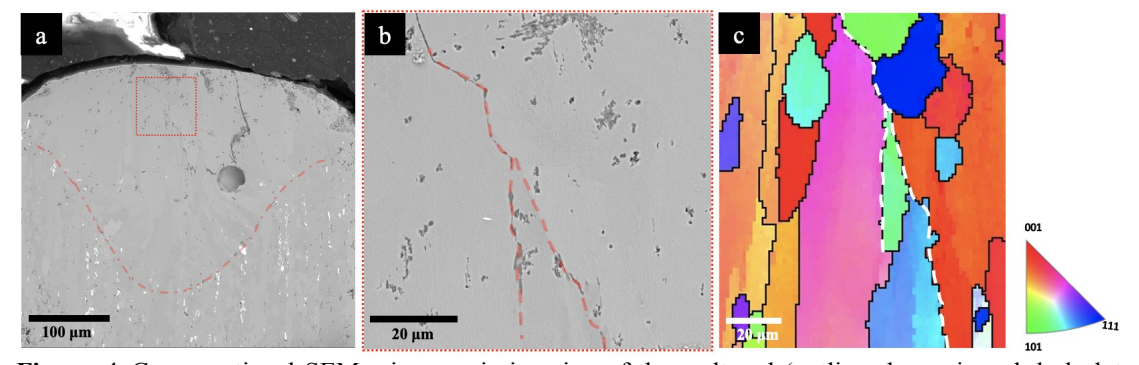


Figure 4. Cross-sectional SEM microscopic imaging of the meltpool (outline shown in red dash-dot line) and crack perpendicular to the laser track (a). (b) shows a higher resolution SEM image of the crack outlined in (a). (c) Corresponding IPF map and crack outline (white dotted line) showing the intergranular nature of the crack propagation. IPF standard triangle is also provided. The corresponding scales are shown in each sub-figure, and the reference direction of the IPF triangle is normal to the cross-sectional plane (i.e., parallel to the laser path).

When a crack forms, it is reasonable to assume that the residual stress is released in the vicinity of the crack bundle. This causes each bundle to be separated by a certain distance from the next one rather than being concentrated in one location [42]. As the solidification front follows behind the heat source of the scanning laser, dendritic growth initiates. Knowing that the freezing range in AA6061 is relatively large (i.e., 70 °C) [43], significant chemical segregation occurs at the solid-liquid interface. This leads to a mushy zone with regions of liquid between dendrites. The liquid inter-dendritic region is not able to accommodate the thermally induced tensile stresses arising from solidification shrinkage in the solid metal, resulting in cracking or tearing of the inter-dendritic regions. At this stage, backfill through narrow inter-dendritic channels is insufficient to compensate and heal the initiated cracks [36], resulting in crack propagation in an interdendritic fashion. Higher energy densities lead to larger meltpools where a greater volume of solidifying metal can create greater stresses leading to more cracking.

Besides cracking, dynamic movement of bubbles during the laser scanning process was also observed. Although some pores escape to the surface due to the combined buoyancy force, the drag force by the Marangoni flow, and the thermocapillary force, others are pinned inside by the solidification front. A careful examination of the DXR results revealed an intriguing phenomenon of cracks initiating from pores, as shown in the cross-sectional view of Error: Reference source not found (d). Figure 5 illustrates this observation as a sequence of DXR images. The movement of a particular bubble (pointed out by the white arrow) along with the melt pool edge (marked with the yellow dotted line) is clearly resolved within our spatiotemporal resolution. The trajectory of this bubble is marked with the red arrow in Fig. 5 (a), showing it moves away from the keyhole towards the rear of the melt pool, likely following the Marangoni flow [44]. While the bubble managed to move freely in the melt pool, it was pinned immediately after the melt pool edge passed over, as depicted in Fig. 5 (b) to Fig. 5 (c).

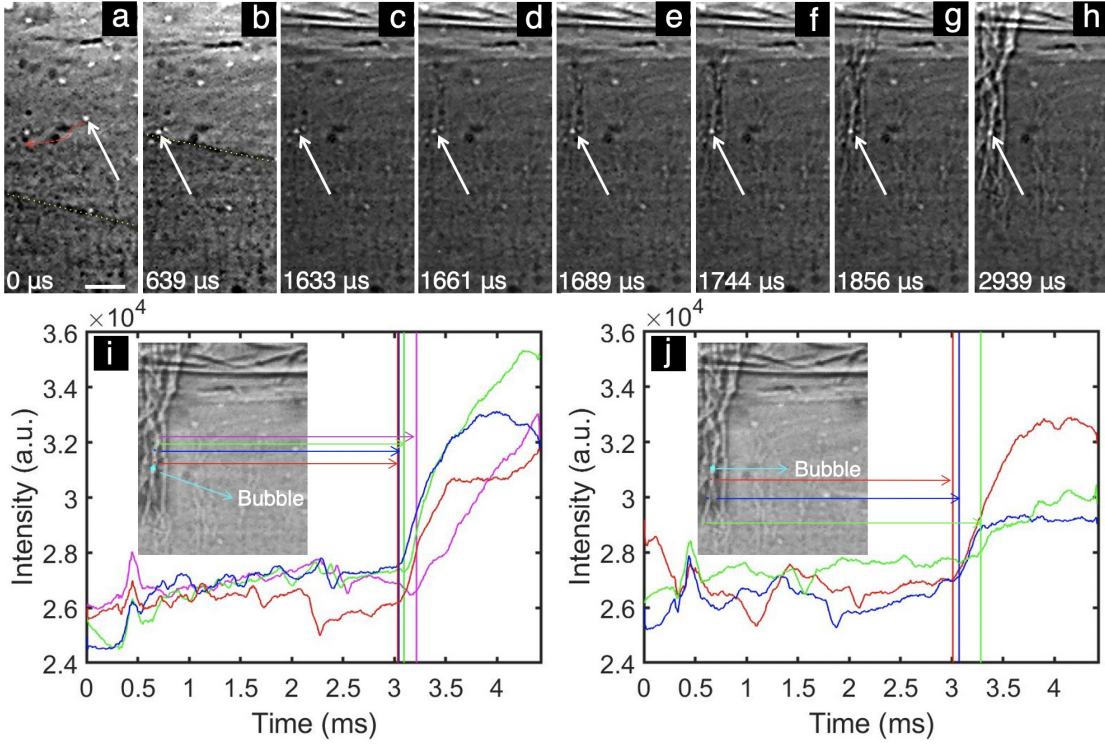


Figure 5. A sequence of DXR images reveals the movement of a bubble and the subsequent cracking initiated from it. The time stamps are labeled to illustrate the relative interval between each sub-figures, while the scale bar is 30 μm. **a)** The bubble of interest is specified by the white arrow, and the red arrow points out where it sits after solidification. The yellow dotted line indicates the trailing edge of the melt pool. **b)** The position of the bubble just before the melt pool edge passed. **c)** The bubble is pinned after the melt pool edge passed. **d)-h)** The initiation and propagation of cracking from the bubble. The change of intensity for (**i)** crack points above the bubble and (**j)** below the bubble during DXR experiment plotted versus time. The inset is the DXR image exhibiting the location of the points and bubble. The vertical lines specify the relative initiation time for each point respectively. The crack propagated upwards above the bubble from the red point to the yellow point in (a), and downwards below the bubble from the red point to the green point in (b).

176 177

178

179

180

181

182

183

184

185

186

187

188

189 190

191

192193

194195

196

197198

199

200

201202

203

204

205206

207

Figure 5 (c-h) shows the initiation of cracking from this bubble and successive stages of propagation. Although further investigation will be required to reveal the influence of pores on the formation of hot cracks on a statistical basis, the observation itself is useful since no model so far to the authors' knowledge has invoked a mechanism of hot cracking originating from pores. Knowing that the temporal resolution of the high-speed images allows the observation of the crack formation, but spatial resolution of our DXR technique limits the observation of the crack tip at its early stage. Therefore, it is challenging to track the initiation and propagation of the crack based on the morphological information provided by the x-ray images. To address this issue, we plotted the time-resolved image intensity variation of each point inside the area of crack of interest to reveal the crack propagation using the technique established in [36], Fig. 5 (i-j). The crack initiation event is revealed as a sudden increase in intensity as x-rays pass through the hot-crack with less attenuation compared to solid material. Analyzing the initiation for each point within the crack reveals the origin and the propagation direction of the crack. The position of the bubble was labeled using light blue marker in Fig. 5 (i-j). Four points above the bubble were marked using red, blue, green and yellow as shown in Fig. 5 (i); while three points below the bubble were marked using red, blue, and green lines & arrows as shown in Fig. 5 (j). Employing the abovementioned analysis, the corresponding frame at initiation time for each point is shown in Fig. 5 (j). It is evident that the

closer the point is to the bubble, the earlier the initiation of the crack, which implies that the crack originated from the bubble, propagating away from it in both directions.

The crack, having initiated from the pore, propagates initially at a high velocity (even higher than the expected solidification rate for AA6061) and then decelerates as it propagates further away from the pore. Specifically, the crack propagation rate from the red to the blue point in Fig. 5 (i) is of the order of 1250 mm/s. The propagation rate decreases drastically to about 165 and 70 mm/s at the green and yellow points, respectively. As for the points below the pore, shown in Fig. 5 (j), the propagation rate from the red to the blue point is around 365 mm/s and decreases to about 135

217 mm/s through the green point.

208

209

210

211

212

213 214

215

216

218

219

220

221

222

223

224

225

226

227

228

229

230

231

232

233

234

235

236 237

238

239 240

241 242

243

244

245

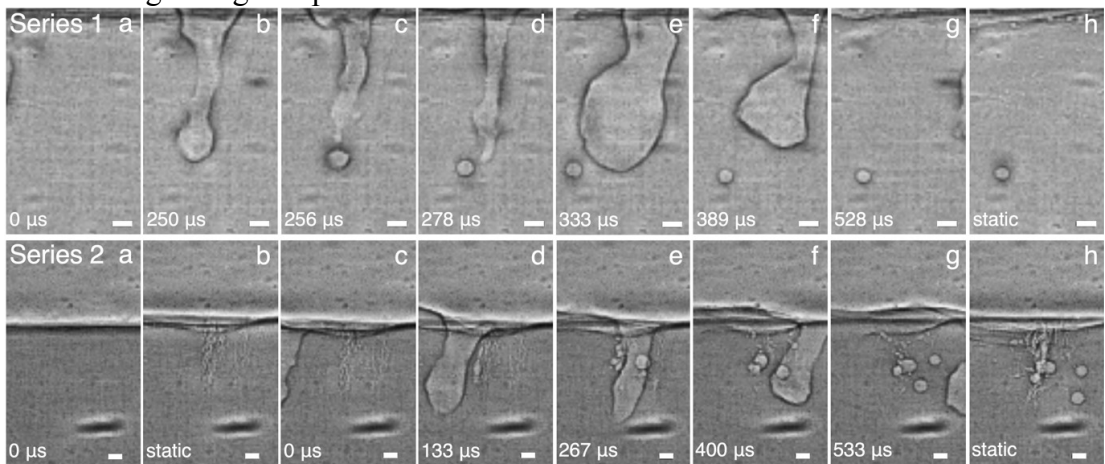


Figure 6. A sequence of DXR images reveals the in situ observation of a pore originating from (Series 1) the collapse of an unstable keyhole and (Series 2) the remelting of pre-existing cracks. (Series 1): Power 368 W and 0.5 m/s scan speed. The instability of keyhole makes its shape and dimension change drastically while moving forward. A sudden snap of the keyhole due to instability leaves a bubble behind if it fails to re-combine with the melt pool before solidification. The time stamps are labeled to illustrate the relative interval between each sub-figure, while the last figure is the static condition after no changes are observed. (Series 2): Power 368 W and 0.6 m/s scan speed. a) The specimen before the first pass of melt pool. b) The resulting cracks after solidification of the first pass. c)-g) The second pass of melt pool liberates the gas inside the existing cracks, which forms bubbles while moving within the melt pool. Some bubbles escape the surface, while others solidify in the substrate. The time interval between the frames is about 13.3 µs. h) A post-experiment radiograph (i.e., static condition) showing the resulting cracks and bubbles after the second pass. All scale bars are equivalent to 30 μm.

It should be mentioned that such pores occur in large quantities but have varied origins. The generation and migration of bubbles during laser melting is a dynamic process that is best characterized with DXR, as for the two cases shown in Fig. 6. In Fig. 6 (Series 1), a sequence of DXR images reveals the dynamic formation process of a pore that pinches off during the fluctuation of an unstable keyhole. A sudden collapse of the keyhole leaves behind a bubble if the pore fails to escape or recombine with the vapor cavity before the material surrounding it solidifies [7]. A keyhole pore of this type is likely to become a favorable site for hot cracking as elaborated above and presented in Figure 5. In another case, pores are generated during remelting of tracks with pre-existing cracks. The first two images in Fig. 6 (Series 2 (a-b)) were taken before and after the first scan of the sample, leaving cracks after solidification. The subsequent images in Fig. 6 (Series 2 (b-h)) show how a second scan of the same hot-cracked sample produces bubbles by liberating the gas inside the existing cracks. There are other means of pore formation such as transfer of gas pores inclusions in the raw powder [45] but those are not in the scope of this discussion. Therefore, understanding the origin and distribution of porosity is a

necessary first step for investigating its relationship with hot cracking or other relating defects resulting from laser-based AM.

Conclusion

248

249

250251

252

253254

255256

257

258

259260

261

262263

264265

266

267

268

269

270

271

272

273

274275

276

277

278279

280

281

282

283

284

285

In summary, we performed *operando* synchrotron x-ray imaging to investigate the hot cracking behavior of AA6061 during the rapid melting and solidification process induced by a high-powder-density laser. The subsurface morphology and distribution of the cracks, formed under different processing parameters pertaining to LPBF, were characterized with unprecedentedly high spatial and temporal resolutions. Our study reveals interesting nature and behavior of the hot cracks. Different from their surface appearance observed using SEM, these hot cracks are in the bundle form underneath the surface with substantial complexity, evidencing the unique solidification behavior of alloys under LPBF conditions. The dimensional analysis of the crack bundles shows that cracks originate near the back of the melt pool and therefore are shallower than the melt pool regardless of the laser condition. The initial crack propagation speed is of order 1 m/s but decreases rapidly during crack propagation. All of these features provide features and data for validation of simulations of hot cracking such as, for example, the variation in hot cracking intensity as a function of linear energy density.

Our study also reveals the significant connection between hot cracks and pores in material. On one hand, pores are favorable sites for crack initiation. This is the case for both large keyhole pores and small pores that pre-exist in the sample. On the other hand, when cracks are present in the material, trapped-gas pores tend to form when the laser beam scans across the cracks, as the gas molecules attached to the crack surface are not able to escape the melt pool. Cracks and pores are common structure defects in LPBF samples. Their strong interaction observed in our study demonstrates the necessity of material-process co-design in advanced manufacturing process. Traditional effort for mitigating the hot cracking issue tend to focus only on tailoring the composition and solidification behavior of the alloy. As indicated here, factors that may cause porosity generation during the laser AM process also need to be given careful considerations. For instances, designing an alloy that is unsusceptible to hot cracking may consider increasing its laser absorption coefficient so that a severe keyholing condition is not necessary for high-efficiency build. Also, absence of precipitates or clusters that consist of volatile elements may be beneficial since the strong evaporation of these elements can create pores.

The direct observations of crack initiation and propagation using *operando* synchrotron x-ray imaging technique will allow the interrogation of many intriguing problems. We believe the experimental results presented here will enable a more rapid development of numerical models and encourage a better integration of efforts on synergistic process-material design and tailoring.

Materials and Methods

- The DXR experiments were conducted at the 32-ID-B beamline of the Advanced
- 287 Photon Source at the Argonne National Laboratory [37]. As shown in Fig. 1, the
- 288 experiment integrates a scanning laser system and a sample chamber into a
- 289 synchrotron x-ray imaging beamline [36,38]. The laser source is ytterbium fiber (IPG
- 290 YLR-500-AC, IPG Photonics, Oxford, Massachusetts, USA), operating with the
- 291 wavelength of 1070 nm at a selected power level from its maximum of 540 W. The

galvo scanner (IntelliSCANde 30, SCANLAB GmbH, Puchheim, Germany) enables the laser to scan across the sample surface at a speed up to 2 m/s. The specimens were enclosed in a stainless steel chamber with 1 atm Ar protective gas.

In this work, experiments were performed using 50 mm long, 3 mm tall and 1 mm thick AA6061 cuboidal specimens with no powder layer on top. While the laser impinged and continued to scan across the long edge of the specimen, the high-energy synchrotron x-rays simultaneously penetrated the thickness of the sample,

- illuminating an area comprising the melt pool and the space above the sample surface.
- A short-period undulator (18 mm) generated polychromatic x-rays with the first
- harmonic energy of 24.4 keV. The incident beam was further collimated using a set of
- 302 slits. A high-speed camera using the CMOS image sensor for faster readout (Photron
- FastCam SA-Z, Photron Inc., Tokyo, Japan) was placed behind the sample chamber to
- record DXR images of the process. The frame rate was 50 kHz and the exposure time
- 305 for each image was 1! s. Two sets of shutters were set in front of the detection
- 306 system to control the x-ray total exposure time for protecting the detector. All the
- 307 DXR images were processed via ImageJ and custom designed "adapthisteq filter" in
- MatlabTM to enhance the contrast so that the features of interest could be visualized more readily.
- For this study, more than 50 experiments were recorded probing the formation of
- 311 hot-cracking in AA6061 at different combinations of laser power and scanning speed.
- The laser power was varied between 50 % and 100 %, equivalent to 254-540 W and
- laser scanning speeds between 0.5 and 0.7 m/s.

314 Acknowledgments

295296

297298

- N.K., R.W.C., and A.D.R. are grateful for the funding from the Department of
- Defense Office of Economic Adjustment award no. ST1605-19-03. G.T. and A.D.R.
- are grateful for the support from the National Science Foundation under grant number
- 318 DMR1905910. This work is supported in part by the Pennsylvania Infrastructure
- 319 Technology Alliance, a partnership of Carnegie Mellon, Lehigh University and the
- 320 Commonwealth of Pennsylvania's Department of Community and Economic
- 321 Development (DCED). This work is also supported in part by the National Aerospace
- and Space Administration (NASA) under grant number 80NSSC19M0123. This
- research used resources of the Advanced Photon Source, a U.S. Department of Energy
- 324 (DOE) Office of Science User Facility operated for the DOE Office of Science by
- 325 Argonne National Laboratory under Contract No. DE-AC02-06CH11357.

326 Reference

- T. Debroy, S.A. David, Physical processes in fusion welding, Rev. Mod. Phys. 67 (1995) 85–112.
- A. Matsunawa, J.-D. Kim, N. Seto, M. Mizutani, S. Katayama, Dynamics of keyhole and molten pool in laser welding, J. Laser Appl. 10 (1998) 247–254.
- 331 [3] C. Zhao, K. Fezzaa, R.W. Cunningham, H. Wen, F. De Carlo, L. Chen, A.D. Rollett, T. Sun, Real-time monitoring of laser powder bed fusion process using
- high-speed X-ray imaging and diffraction, Sci. Rep. (2017).
- H. Gong, K. Rafi, H. Gu, T. Starr, B. Stucker, Analysis of defect generation in Ti-6Al-4V parts made using powder bed fusion additive manufacturing processes, Addit. Manuf. 1 (2014) 87–98.
- 337 [5] N.T. Aboulkhair, N.M. Everitt, I. Ashcroft, C. Tuck, Reducing porosity in

- AlSi10Mg parts processed by selective laser melting, Addit. Manuf. 1 (2014) 77–86.
- W.E. King, H.D. Barth, V.M. Castillo, G.F. Gallegos, J.W. Gibbs, D.E. Hahn,
 C. Kamath, A.M. Rubenchik, Observation of keyhole-mode laser melting in
 laser powder-bed fusion additive manufacturing, J. Mater. Process. Technol.
 214 (2014) 2915–2925.
- R. Cunningham, C. Zhao, N. Parab, C. Kantzos, J. Pauza, K. Fezzaa, T. Sun, A.D. Rollett, Keyhole threshold and morphology in laser melting revealed by ultrahigh-speed x-ray imaging, Science (80-.). 363 (2019) 849–852.
- 347 [8] M. Tang, P.C. Pistorius, J.L. Beuth, Prediction of lack-of-fusion porosity for powder bed fusion, Addit. Manuf. 14 (2017) 39–48.
- H.E. Sabzi, P.E.J. Rivera-Díaz-del-Castillo, Defect prevention in selective laser melting components: Compositional and process effects, Materials (Basel). 12 (2019).
- S.S. Sames, W.J., List, F.A., Pannala, S., Dehoff, R.R. and Babu, The metallurgy and processing science of metal additive manufacturing, Int. Mater. Rev. 5 (2016) 315–360.
- J.P. Kruth, G. Levy, F. Klocke, T.H.C. Childs, Consolidation phenomena in laser and powder-bed based layered manufacturing, CIRP Ann. Manuf. Technol. 56 (2007) 730–759.
- I. Yadroitsev, A. Gusarov, I. Yadroitsava, I. Smurov, Single track formation in selective laser melting of metal powders, J. Mater. Process. Technol. (2010).
- D. Gu, Y. Shen, Balling phenomena in direct laser sintering of stainless steel powder: Metallurgical mechanisms and control methods, Mater. Des. (2009).
- N.K. Tolochko, Y. V. Khlopkov, S.E. Mozzharov, M.B. Ignatiev, T. Laoui,
 V.I. Titov, Absorptance of powder materials suitable for laser sintering, Rapid
 Prototyp. J. 6 (2000) 155–161.
- T. Qi, H. Zhu, H. Zhang, J. Yin, L. Ke, X. Zeng, Selective laser melting of
 Al7050 powder: Melting mode transition and comparison of the characteristics
 between the keyhole and conduction mode, Mater. Des. (2017).
- [16] M.L. Montero Sistiaga, R. Mertens, B. Vrancken, X. Wang, B. Van
 Hooreweder, J.P. Kruth, J. Van Humbeeck, Changing the alloy composition of
 Al7075 for better processability by selective laser melting, J. Mater. Process.
 Technol. (2016).
- N. Kaufmann, M. Imran, T.M. Wischeropp, C. Emmelmann, S. Siddique, F. Walther, Influence of process parameters on the quality of aluminium alloy en AW 7075 using Selective Laser Melting (SLM), in: Phys. Procedia, 2016.
- [18] H. Zhang, H. Zhu, T. Qi, Z. Hu, X. Zeng, Selective laser melting of high
 strength Al-Cu-Mg alloys: Processing, microstructure and mechanical
 properties, Mater. Sci. Eng. A. (2016).
- N.J. Harrison, I. Todd, K. Mumtaz, Reduction of micro-cracking in nickel superalloys processed by Selective Laser Melting: A fundamental alloy design approach, Acta Mater. 94 (2015) 59–68.
- 381 [20] S.Z. Uddin, L.E. Murr, C.A. Terrazas, P. Morton, D.A. Roberson, R.B. Wicker, 382 Processing and characterization of crack-free aluminum 6061 using high-383 temperature heating in laser powder bed fusion additive manufacturing, Addit. 384 Manuf. 22 (2018) 405–415.
- L. N. Carter, M. M. Attallah, R. C. Reed, Laser powder bed fabrication of nickel-base superalloys: influence of parameters; characterisation, quantification and mitigation of cracking, Superalloys 2012. (2012) 577--586.

- A. Röttger, K. Geenen, M. Windmann, F. Binner, W. Theisen, Comparison of microstructure and mechanical properties of 316 L austenitic steel processed by selective laser melting with hot-isostatic pressed and cast material, Mater. Sci. Eng. A. 678 (2016) 365–376.
- H. Wang, X. Zhang, G.B. Wang, J. Shen, G.Q. Zhang, Y.P. Li, M. Yan, Selective laser melting of the hard-to-weld IN738LC superalloy: Efforts to mitigate defects and the resultant microstructural and mechanical properties, J. Alloys Compd. 807 (2019).
- 396 [24] M. Miyagi, Y. Kawahito, H. Wang, H. Kawakami, T. Shoubu, M. Tsukamoto, X-ray phase contrast observation of solidification and hot crack propagation in laser spot welding of aluminum alloy, Opt. Express. 26 (2018) 22626.
- M. Miyagi, Y. Kawahito, H. Kawakami, T. Shoubu, Direct observation of weld pool formation and cracking in laser welding of Al alloy by using x-ray phase contrast method, 402 (2019) 402.
- D.G. Eskin, L. Katgerman, A quest for a new hot tearing criterion, Metall. Mater. Trans. A Phys. Metall. Mater. Sci. 38 A (2007) 1511–1519.
- N. Coniglio, C.E. Cross, Initiation and growth mechanisms for weld solidification cracking, Int. Mater. Rev. 58 (2013) 375–397.
- Suyitno, W.H. Kool, L. Katgerman, Hot tearing criteria evaluation for directchill casting of an Al-4.5 pct Cu alloy, Metall. Mater. Trans. A Phys. Metall. Mater. Sci. 36 (2005) 1537–1546.
- D.G. Eskin, Suyitno, L. Katgerman, Mechanical properties in the semi-solid state and hot tearing of aluminium alloys, Prog. Mater. Sci. 49 (2004) 629–711.
- [30] M. Rappaz, J.M. Drezet, M. Gremaud, A new hot-tearing criterion, Metall.
 Mater. Trans. A Phys. Metall. Mater. Sci. 30 (1999) 449–455.
- 413 [31] S. Kou, A criterion for cracking during solidification, Acta Mater. 88 (2015) 366–374.
- 415 [32] A. Niel, C. Bordreuil, F. Deschaux-Beaume, G. Fras, Modelling hot cracking in 6061 aluminium alloy weld metal with microstructure based criterion, Sci. Technol. Weld. Join. 18 (2013) 154–160.
- H.R. Zareie Rajani, A.B. Phillion, 3D multi-scale multi-physics modelling of hot cracking in welding, Mater. Des. 144 (2018) 45–54.
- 420 [34] M. Rohde, C. Markert, W. Pfleging, Laser micro-welding of aluminum alloys: 421 Experimental studies and numerical modeling, Int. J. Adv. Manuf. Technol. 50 422 (2010) 207–215.
- [35] C. Hagenlocher, D. Weller, R. Weber, T. Graf, Analytical Description of the
 Influence of the Welding Parameters on the Hot Cracking Susceptibility of
 Laser Beam Welds in Aluminum Alloys, Metall. Mater. Trans. A Phys. Metall.
 Mater. Sci. 50 (2019) 5174–5180.
- P. Chiang, R. Jiang, R. Cunningham, N. Parab, C. Zhao, K. Fezzaa, T. Sun,
 A.D. Rollett, In Situ Characterization of Hot Cracking Using Dynamic X-Ray
 Radiography, Springer International Publishing, 2019.
- [37] N.D. Parab, C. Zhao, R. Cunningham, L.I. Escano, K. Fezzaa, W. Everhart,
 A.D. Rollett, L. Chen, T. Sun, Ultrafast X-ray imaging of laser-metal additive
 manufacturing processes, J. Synchrotron Radiat. 25 (2018) 1467–1477.
- 433 [38] C. Zhao, K. Fezzaa, R.W. Cunningham, H. Wen, F. De Carlo, L. Chen, A.D. Rollett, T. Sun, Real-time monitoring of laser powder bed fusion process using high-speed X-ray imaging and diffraction, Sci. Rep. 7 (2017) 1–11.
- Q. Guo, C. Zhao, L.I. Escano, Z. Young, L. Xiong, K. Fezzaa, W. Everhart, B.
 Brown, T. Sun, L. Chen, Transient dynamics of powder spattering in laser

- powder bed fusion additive manufacturing process revealed by in-situ highspeed high-energy x-ray imaging, Acta Mater. 151 (2018) 169–180.
- 440 [40] Q. Guo, C. Zhao, M. Qu, L. Xiong, L.I. Escano, S.M.H. Hojjatzadeh, N.D. Parab, K. Fezzaa, W. Everhart, T. Sun, L. Chen, In-situ characterization and quantification of melt pool variation under constant input energy density in laser powder bed fusion additive manufacturing process, Addit. Manuf. 28 (2019) 600–609.
- 445 [41] B. Meylan, T. Le-Quang, M.P. Olbinado, A. Rack, S.A. Shevchik, K. Wasmer, Re-solidification dynamics and microstructural analysis of laser welded aluminium, Int. J. Mater. Res. 111 (2020) 17–22.
- [42] N.F. Mott, Fragmentation of Shell Cases, Proc. R. Soc. Lond. A. Math. Phys.
 Sci. 189 (1947) 300–308.
- 450 [43] C.E. Roberts, D. Bourell, T. Watt, J. Cohen, A novel processing approach for 451 additive manufacturing of commercial aluminum alloys, Phys. Procedia. 83 452 (2016) 909–917.
- [44] N. Kouraytem, X. Li, R. Cunningham, C. Zhao, N. Parab, T. Sun, A.D. Rollett,
 A.D. Spear, W. Tan, Effect of Laser-Matter Interaction on Molten Pool Flow
 and Keyhole Dynamics, Phys. Rev. Appl. 11 (2019) 1–16.
- 456 [45] R. Cunningham, S.P. Narra, C. Montgomery, J. Beuth, A.D. Rollett,
 457 Synchrotron-Based X-ray Microtomography Characterization of the Effect of
 458 Processing Variables on Porosity Formation in Laser Power-Bed Additive
 459 Manufacturing of Ti-6Al-4V, Jom. 69 (2017) 479–484.
 460